Morphological Instability of Grain Boundaries in Two-Phase Coherent Solids

Pierre-Antoine Geslin,[*] Yechuan Xu, and Alain Karma[†]
Physics Department and Center for Interdisciplinary Research on Complex Systems,
Northeastern University, Boston, Massachusetts 02115, USA

We show both computationally and analytically that grain boundaries that exhibit shear-coupled motion become morphologically unstable in solid alloys that phase separate into coherent domains of distinct chemical compositions. We carry out simulations of continuum models demonstrating that this instability is mediated by long-range elastic interaction between compositional domains and grain boundaries. In addition, we perform a linear stability analysis that predicts the range of unstable wavelengths in good quantitative agreement with simulations. In nonlinear stages, this pattern-forming instability leads to the breakup of low-angle grain boundaries, thereby strongly impacting microstructural evolution in a wide range of phase-separating materials.

Grain boundaries (GBs) can strongly influence the mechanical and functional behavior of a wide range of crystalline materials and have been widely studied for this reason [1,2]. The last decade, in particular, has witnessed major progress in understanding and characterizing the response of GBs to applied stress [3–15]. A key feature of this response is the *coupling* between GB motion normal to the GB plane and a shear deformation parallel to this plane, characterized by the relation

$$v_\parallel = \beta v_n \tag{1}$$

between the GB normal velocity v_n, and the velocity $v_\parallel$ of parallel grain translation, where β is a coupling factor that depends on GB bicrystallography [3,4]. For low-angle GBs consisting of individual dislocations, coupling follows from the geometrical relation between dislocation glide motion and crystal lattice translation [1,3]. For high-angle GBs with atomically disordered intergranular structures, the existence of this relation is less intuitive. However, remarkably, a wide range of high-angle GBs has been shown both computationally and experimentally to exhibit coupling [4–11], making it a general phenomenon. Coupling has also been shown to influence the mechanical and coarsening behaviors of both small and large assemblies of fine grains [9,12,13,16,17]. Those studies have focused primarily on single-phase polycrystalline materials.

In this Letter, we highlight the fundamental role of GB coupling in a different, albeit very common, situation where stress is generated internally by phase separation into domain structures of distinct chemical compositions. Those structures can form by nucleation and growth of a second phase precipitate inside the matrix of a primary phase [18] or by spinodal decomposition into two phases, which have been widely investigated in various contexts [19–29]. Domain formation generates a *coherency* stress due to the dependence of the crystal lattice spacing on composition. This stress is theoretically understood to influence spinodal decomposition differently inside the bulk of a material [19] and near free surfaces that can relax the coherency stress [27]. However, how coherency stress affects GB evolution remains poorly understood fundamentally. Here we demonstrate that a static planar GB can become spontaneously unstable morphologically due to its elastic interaction with compositional domain boundaries (DBs) and its coupling behavior that provides a stress relaxation mechanism. Importantly, the shear stress that drives GB motion is generated by the instability itself, as opposed to being externally applied as in the traditional setting in which coupling has been primarily studied to date [3–15].

We model the evolution of the concentration field using standard conserved dynamics

$$\partial_t c = M \nabla^2 \frac{\delta F}{\delta c}, \tag{2}$$

derived from an energy functional

$$\mathcal{F} = \int dV \left[f_{\mathrm{dw}}(c) + \frac{K}{2} |\nabla c|^2 + f_{\mathrm{el}}(c, \ldots) \right], \tag{3}$$

which represents the total free-energy of the system. The free-energy density is the sum of two parts. The first chemical part of the Cahn-Hilliard form [30] is the sum of a symmetric double-well potential $f_{\mathrm{dw}}(c)$ with minima at c_0^+ and c_0^- and a gradient square term, which together determine the excess compositional DB free-energy γ. The second part is the elastic contribution $f_{\mathrm{el}}(c, \ldots)$ where "…" signifies auxiliary variables used to model elasticity in two ways. A first approach is a nonlinear elastic model (NLEM) where the auxiliary variables are components of

the strain tensor ε_{ij} with the form of $f_{\rm el}(c, \varepsilon_{ij})$ chosen to be periodic in ε_{xy} so as to naturally describe dislocation glide for low-angle GBs on a simple cubic lattice [31,32]. This form is also chosen to describe the interaction between composition and stress such that, in the bulk crystal away from dislocations, $f_{\rm el}(c, \varepsilon_{ij}) \approx \frac{1}{2}\sigma_{ij}(\varepsilon_{ij} - \varepsilon_{ij}^0 c)$ where $\varepsilon_{ij}^0 = \varepsilon_0 \delta_{ij}$ is the dilatational stress-free eigenstrain that incorporates a linear dependence of the lattice spacing on composition (Vegard's law), and elasticity is modeled isotropically with shear modulus G and Poisson's ratio ν. In the second approach based on amplitude equations (AE) [33–35], the auxiliary variables are complex amplitudes A_n of density waves in an expansion of the crystal density field $n(\vec{r}, t) = n_0 + \delta n_s \sum_{n=1}^{3} 2\Re[A_n e^{i\vec{k}_n \cdot \vec{r}}]$, where $\Re$ denotes the real part. We choose the form of $f_{\rm el}(c, \{A_n\}, \{A_n^*\})$ from Ref. [35] that also reduces to isotropic elasticity with Vegard's law in the bulk and the set of principal reciprocal lattice vectors k_n of the two-dimensional hexagonal lattice. Both models also describe dislocation glide and hence GB coupling via Eq. (1) with $\beta \approx \theta$ for small misorientation [3,4]. The AE approach has the additional feature of also describing dislocation climb as in the PFC model [36]. In both models, the mechanical fields are relaxed on a much shorter time scale than the composition field, such that the strain fields and the GB position are always close to their equilibrium value on the time scale of the precipitate evolution. Further details of the models and simulations are given in [37].

Results of simulations illustrating the instability of a low-angle symmetric tilt GB for a 7.12° misorientation are shown in Fig. 1. These simulations are performed for a generic set of materials parameters ($c_0^- = 0.05$, $c_0^+ = 0.95$, $G = 40$ GPa, $\nu = 0.25$, $\varepsilon_0 = 4.3\%$, and $\gamma = 163$ mJ/m^2) similar to the ones used to model phase separation in Li-ion battery materials [27,38]. We focus on a geometry in which a planar grain boundary is initially centered inside a lamellar precipitate. This choice of geometry is physically motivated by the fact that dislocations act as preferred sites of nucleation [39–41] and, hence, GBs naturally seed the formation of lamellar precipitates of this approximate geometry [20,42]. Figure 1 shows that small sinusoidal perturbations of both the GB and DBs become simultaneously amplified with the GB modulation being phase shifted spatially by $\pi/4$ from the in-phase modulations of both DBs. When the amplitude of the GB modulation exceeds a critical value, the GB breaks up [Figs. 1(c) and 1(g)] and dislocations become anchored at the precipitate interfaces, thereby relaxing the coherency stress. The last frames of both simulations [Figs. 1(d) and 1(h)] are similar, presenting zigzag shaped precipitates with serrated interfaces due to the dislocations stress fields. Both simulation methods yield identical initial destabilization stages, which are mediated solely by dislocation glide, but differ in the nonlinear stages after breakup. Without climb,
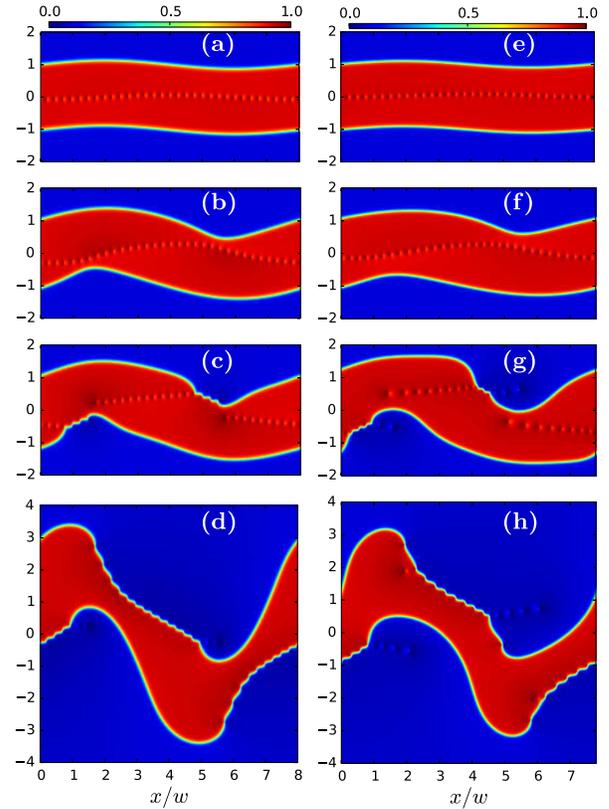
FIG. 1 (color online).   Color plots of the composition field c at different times increasing from top to bottom in NLEM (a),(b), (c),(d) and AE (e),(f),(g),(h) simulations illustrating the destabilization of a low-angle GB ($\theta = 7.12°$). Simulated domains with periodic boundary conditions in x have a size $L_x \times L_y$ of $8w \times 32w$ ($7.8w \times 11.3w$) for NLEM (AE) where $2w$ is the initial distance between compositional DBs (the vertical size of each frame is smaller than L_y). See Supplemental Material [37] for full movies of these simulations.

the NLEM simulation leads to a frustrated configuration while with climb the AE simulation further relaxes this configuration by adjustments of dislocation spacings. We note that climb generally occurs on a much larger time scale than glide in real systems, while these two mechanisms occur on a comparable time scale in the AE simulations. However, this difference affects neither the initial stage of the instability, which is dominated by glide, nor the final relaxed equilibrium configuration [Fig. 1(h)] that corresponds to a global free-energy minimum.

The instability mechanism can be qualitatively understood by noting that a small initial sinusoidal perturbation of DBs of wavelength Λ depicted in Fig. 2 is stable in the absence of GB inside the precipitate. This is because this perturbation increases the total DB energy ($= \gamma \times$ total DB length), but leaves the elastic energy unchanged since elasticity is assumed isotropic and the entire solid domain is periodic in x and infinite in y ($L_y \gg \Lambda$). Therefore, according to the Bitter-Crum theorem [43,44], the elastic energy depends only on the volume of precipitate, which is
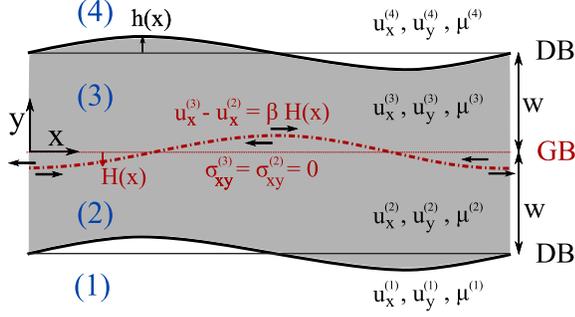
FIG. 2 (color online). Schematic representation of a GB sandwiched between two perturbed compositional DBs distinguishing four regions (numbered 1 to 4) and displacement fields used in the stability analysis. The horizontal arrows show the directions of grain translation resulting from GB coupled motion via Eq. (1), which relaxes the shear stress induced by the DB perturbation.

constant by Eq. (2), but is independent of its shape. In contrast, with a GB present, the elastic energy can be decreased by the relaxation of the shear stress induced by the DB perturbation along the GB plane ($y = 0$) via GB coupled motion. Therefore, we expect the existence of a stability length Λ_s, such that long-wavelength perturbations ($\Lambda > \Lambda_s$) are amplified by stress relaxation and short-wavelength perturbations ($\Lambda < \Lambda_s$) are stabilized by the DB energy γ. This mechanism bears some similarities with the Asaro-Tiller-Grinfeld (ATG) instability [45,46], where the destabilization of a film deposited on a substrate is mediated by the relaxation of the normal stresses at the free surface. The present instability presents, however, a different geometry and is mediated by the relaxation of the shear stress at the GB.

We now carry out a linear stability analysis to predict Λ_s and we validate the prediction by simulations. We outline the main steps of the analysis that treats the GB and DBs as sharp interfaces and provide details in the Supplemental Material [37]. We first calculate the nonperturbed solutions of static elasticity for planar GB and DBs. Imposing the continuity of displacements and stress vector components $T_i = \sigma_{ij} n_j$ across the DBs, where $\mathbf{n} = [n_x, n_y]$ is the interface normal, we find the elastic displacements $\bar{u}_x^{(m)} = 0$ ($m = 1$ to 4) and

$$\bar{u}_y^{(1)}(y) = \frac{\varepsilon_0}{1 - \nu}(c^-(y + w) + c^+ w),$$

$$\bar{u}_y^{(m)}(y) = \frac{\varepsilon_0}{1 - \nu}c^+ y, \qquad m = 2, 3 \qquad (4)$$

$$\bar{u}_y^{(4)}(y) = \frac{\varepsilon_0}{1 - \nu}(c^-(y - w) + c^+ w),$$

where the numbers in superscript refer to different regions depicted in Fig. 2. The unperturbed chemical potential $\bar{\mu}$ is constant, and the compositions $\bar{c}^\pm$ in each domain differ from the minima $c_0^\pm$ of $f_{\mathrm{dw}}(c)$ because of the

unperturbed stresses $\bar{\sigma}_{xx}^{(m)}$ and $\bar{\sigma}_{yy}^{(m)}$ that can be computed from Eq. (4).

Next, we consider the perturbed problem where the heights of the DBs and the GB perturbations are slowly varying functions of x denoted by $h(x)$ and $H(x)$, respectively (Fig. 2). We write accordingly the perturbed chemical potential, displacement fields, and stress fields as $\mu^{(m)} = \bar{\mu} + \tilde{\mu}^{(m)}$, $u_i^{(m)} = \bar{u}_i^{(m)} + \tilde{u}_i^{(m)}$, $\sigma_{ij}^{(m)} = \bar{\sigma}_{ij}^{(m)} + \tilde{\sigma}_{ij}^{(m)}$, respectively, where quantities with the superscript tilde are small perturbed quantities. From a sharp-interface-limit analysis of Eqs. (2)–(3) including stress effects, we obtain a set of equations and boundary conditions governing the coupled evolution of the perturbed fields and interfaces [37]:

$$\partial_t \tilde{\mu}^{(m)} = D\nabla^2 \tilde{\mu}^{(m)}, \qquad m = 1, \ldots, 4, \qquad (5)$$

$$\tilde{\mu}_{\mathrm{DB}} = -\varepsilon_0(\tilde{\sigma}_{xx} + \tilde{\sigma}_{yy}) + \frac{\gamma\kappa}{\Delta\bar{c}}, \qquad [\![\tilde{\mu}]\!]_{\mathrm{GB}} = 0 \qquad (6)$$

$$v_{\mathrm{DB}} = -\frac{M}{\Delta\bar{c}}[\![\partial_y \mu]\!]_{\mathrm{DB}}, \qquad (7)$$

$$\partial_j \sigma_{ij} = 0, \qquad i = x, y, \qquad (8)$$

$$[\![u_i]\!]_{\mathrm{DB}} = 0, \qquad [\![T_i]\!]_{\mathrm{DB}} = 0, \qquad i = x, y, \qquad (9)$$

$$[\![u_x]\!]_{\mathrm{GB}} = \beta H(x, t), \qquad (10)$$

$$[\![u_y]\!]_{\mathrm{GB}} = 0, \qquad [\![T_y]\!]_{\mathrm{GB}} = 0. \qquad (11)$$

$$T_x^{(m)}(x, H(x, t)) = 0, \qquad m = 2, 3, \qquad (12)$$

where $D = Mf''(\bar{c}^\pm)$ is the solute diffusivity, $\Delta\bar{c} = \bar{c}^+ - \bar{c}^-$, and κ is the DB curvature. In addition, double square brackets indicate the jump of a quantity across a given interface type (GB or DB) labeled in subscript (e.g., $[\![\tilde{\mu}]\!]_{\mathrm{GB}} = \tilde{\mu}_{\mathrm{GB}}^{(3)} - \tilde{\mu}_{\mathrm{GB}}^{(2)} = 0$).

To compute the stability spectrum, we assume a perturbation of the form $h(x, t) = h_i e^{\omega_k t}\sin(kx)$ and solve Eqs. (5)–(12) to determine the amplification rate ω_k of perturbations. We first solve the elastostatic equations (8) subject to known boundary conditions for the displacement and stress fields at the GB and DBs. Those include, at the DBs, the continuity of displacements and stress vector (9) and, at the GB, the jump of tangential displacement (10) that follows from the GB coupling relation (1) (see [10]), the continuity of normal displacement and normal stress (11), and (12) which assumes that the GB adapts its shape instantaneously via coupling to completely relax the shear stress on the GB. This assumption is physically justified by the fact that diffusion-controlled DB motion is typically much slower than dislocation-glide-mediated GB motion, also valid for the NLEM and AE simulations. The solutions of the elastostatic equations (8) for the perturbative

displacement fields $\tilde{u}_i^{(m)}$ have 4 unknown constants in domains (2) and (3), but only 2 unknown constants in domains (1) and (4) due to the boundary conditions $\tilde{u}_i^{(1)}(-\infty) = \tilde{u}_i^{(4)}(+\infty) = 0$. The 13 boundary conditions (9)–(12) determine those 12 unknowns together with the amplitude of the GB modulation. We obtain

$$H(x,t) = -\frac{4h_i\varepsilon_0\Delta\bar{c}}{\beta}e^{-kw}e^{\omega_k t}\cos(kx), \qquad (13)$$

where the phase shift between the $\cos(kx)$ GB modulation and the $\sin(kx)$ DB modulation, observed in simulations (Fig. 1), is a direct consequence of the shear stress relaxation on the GB plane.

The stability spectrum is now readily obtained by using the elastostatic solutions to compute the stress contribution to the shift of chemical potential on the two DBs using the local equilibrium condition (6) evaluated at $y = \pm w$. This yields $\tilde{\mu}_{DB}(x, y = \pm w, t) = \pm\Gamma(k)h(x,t)$, where

$$\Gamma(k) = \frac{4G\varepsilon_0^2\Delta\bar{c}}{1-\nu}(ke^{-2kw} - 2d_0k^2), \qquad (14)$$

and terms $\sim ke^{-2kw}$ and $\sim d_0k^2$ represent the contribution of stresses and DB curvature, respectively; $d_0 = \gamma(1-\nu)/8G\varepsilon_0^2\Delta\bar{c}^2$ is a microscopic length that is the ratio of the DB energy and an elastic energy (e.g., for the parameters of the simulations $d_0 = 0.297$ nm). Solutions of the diffusion equation (5) in different regions subject to the conditions $\tilde{\mu}_{DB}(x, y = \pm w, t) = \pm\Gamma(k)h(x,t)$ are

$$\tilde{\mu}^{(1)} = \Gamma(k)e^{q(y+w)}h(x,t)$$

$$\tilde{\mu}^{(m)} = -\Gamma(k)\frac{\sinh(qy)}{\sinh(qw)}h(x,t), \qquad m = 2,3,$$

$$\tilde{\mu}^{(4)} = -\Gamma(k)e^{-q(y-w)}h(x,t), \qquad (15)$$

where $q = \sqrt{k^2 + \omega_k/D}$. Finally, substituting those solutions into the mass conservation condition (7), which implies that $v_{int} = \partial_t h = \omega_k h$, and using the quasistatic approximation $q \approx k$ valid in the limit $\omega_k \ll Dk^2$ of our simulations, we obtain

$$\omega_k = \frac{M\Gamma(k)k}{\Delta\bar{c}}(1 + \coth(kw)). \qquad (16)$$

Confirming the qualitative picture of the instability mechanism discussed earlier, long (short) wavelength perturbations for $k < k_s$ ($k > k_s$) are unstable (stable). The marginally stable mode corresponding to $\omega_k = 0$ can be computed analytically by setting $\Gamma(k_s) = 0$, which yields

$$k_s = \frac{2\pi}{\Lambda_s} = \frac{1}{2w}W_L(w/d_0), \qquad (17)$$

where W_L is the Lambert function [47]. We compare in Fig. 3 the analytical predictions of Eq. (16) for ω_k, Eq. (17) for k_s, and the fastest growing wave number k_0 computed from Eq. (16) by solving $d\omega_k/dk = 0$, to results of NLEM and AE simulations, where ω_k was computed by fitting the amplitude of sinusoidal perturbation of interfaces to growing or decaying exponential functions of time for different k's. The comparison shows an excellent quantitative agreement, thereby validating the analysis. Furthermore, in the physically relevant limit where the precipitate width is much larger than the microscopic capillary length ($w \gg d_0$), the asymptotic behavior of the Lambert function implies that $k_s \approx (1/2w)\ln(w/d_0)$. In addition, k_0 is the solution of the transcendental equation $k_0w[1 + \coth(k_0w)] = 2$, yielding $k_0 \approx C/w$ where C is a numerical constant ($C = 0.797\ldots$). This implies that in this limit the fastest growing wavelength $\Lambda_0 \sim w$, while $\Lambda_s \sim w/\ln(w/d_0) \ll \Lambda_0$. For $w \sim 100$ nm and lower misfit than simulated here, e.g., $\varepsilon_0 = 0.2\%$, the above relation yields the estimate $\Lambda_s \sim 1$ μm. Since precipitates typically extend spatially along the GB plane a distance of the order of a few micrometers, the instability should also appear for small misfits.

This instability should affect more strongly low angle GBs because of the inverse relation between the GB deformation amplitude H and β [Eq. (13)], causing the breakup of GBs with small β in nonlinear stages as seen in the simulations (Fig. 1). However, it will also impact
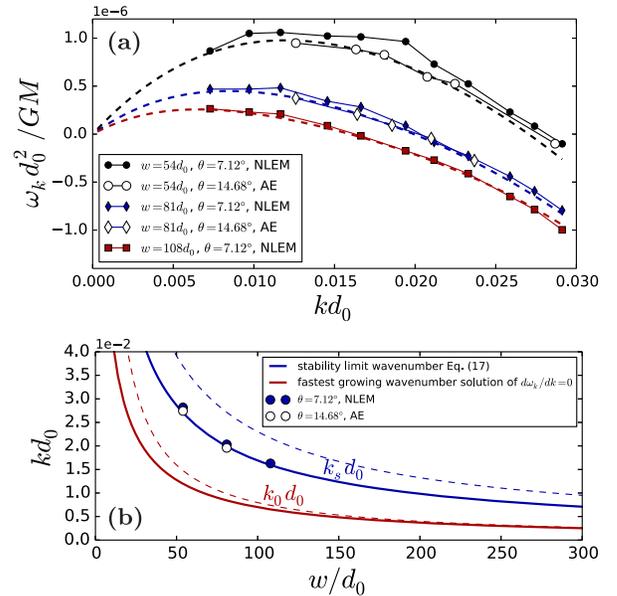
FIG. 3 (color online).   (a) Comparison of dimensionless growth rate $\omega_k d_0^2/(GM)$ versus dimensionless wave number kd_0 from Eq. (16) (dashed lines) and from simulations of NLEM (full symbols) and AE methods (hollow symbols). (b) Marginal (k_s) and fastest growing (k_0) wave numbers (full lines) normalized by d_0 versus w/d_0 and their asymptotic behaviors for $w \gg d_0$ (dashed lines).

precipitate evolution in the presence of high-angle GBs that couple as well as GBs exhibiting mixed coupling and sliding or pure sliding [4,9,10]. This is because the growth rate of instability (ω_k) is independent of β and hence misorientation as validated by simulations (Fig. 3). Hence, a GB that purely slides will not deform but still relax a shear stress leading to destabilization of DBs. Even though we highlighted here the instability for lamellar precipitates, a similar analysis shows that a GB adjacent to a single DB belonging to a large precipitate is subject to the same instability.

The present linear stability analysis is a first step towards understanding the complex interaction between GBs and precipitates formed by nucleation or spinodal decomposition in a wide range of two-phase materials. For example, in Ni-Al superalloys, the nucleation and growth of γ' GB precipitates have been shown to be responsible for GB serration [48,49]. Another example is the formation of acicular Widmanstätten precipitates from GBs, common in steel and Ti alloys. The nucleation and early stages of growth of those precipitates remain largely unknown despite recent clarifications of their stationary growth regime [50]. We expect that it should be possible to validate directly experimentally salient features of the instability mechanism demonstrated in this Letter by precise *in situ* observations of precipitate growth on GBs.

[*]p.geslin@neu.edu

[†]a.karma@neu.edu

[1] A. Sutton and R. Balluffi, *Interfaces in Crystalline Materials* (Oxford Univ. Press, Oxford, 1995).

[2] Y. Mishin, M. Asta, and J. Li, Acta Mater. **58**, 1117 (2010).

[3] J. Cahn and J. Taylor, Acta Mater. **52**, 4887 (2004).

[4] J. Cahn, Y. Mishin, and A. Suzuki, Acta Mater. **54**, 4953 (2006).

[5] V. A. Ivanov and Y. Mishin, Phys. Rev. B **78**, 064106 (2008).

[6] T. Gorkaya, D. Molodov, and G. Gottstein, Acta Mater. **57**, 5396 (2009).

[7] D. Olmsted, E. Holm, and S. Foiles, Acta Mater. **57**, 3704 (2009).

[8] D. Molodov, T. Gorkaya, and G. Gottstein, J. Mater. Sci. **46**, 4318 (2011).

[9] Z. Trautt, A. Adland, A. Karma, and Y. Mishin, Acta Mater. **60**, 6528 (2012).

[10] A. Karma, Z. T. Trautt, and Y. Mishin, Phys. Rev. Lett. **109**, 095501 (2012).

[11] A. Rajabzadeh, F. Mompiou, S. Lartigue-Korinek, N. Combe, M. Legros, and D. Molodov, Acta Mater. **77**, 223 (2014).

[12] T. Rupert, D. Gianola, Y. Gan, and K. Hemker, Science **326**, 1686 (2009).

[13] J. Sharon, P. Su, F. Prinz, and K. Hemker, Scr. Mater. **64**, 25 (2011).

[14] M. Winning, A. Rollett, G. Gottstein, D. Srolovitz, A. Lim, and L. Shvindlerman, Philos. Mag. **90**, 3107 (2010).

[15] A. Lim, M. Haataja, W. Cai, and D. Srolovitz, Acta Mater. **60**, 1395 (2012).

[16] K.-A. Wu and P. Voorhees, Acta Mater. **60**, 407 (2012).

[17] A. Adland, Y. Xu, and A. Karma, Phys. Rev. Lett. **110**, 265504 (2013).

[18] D. Porter and K. Easterling, *Phase Transformations in Metals and Alloys, (Revised Reprint)* (CRC Press, Boca Raton, 1992).

[19] J. Cahn, Acta Metall. **9**, 795 (1961).

[20] H. Ramanarayan and T. Abinandanan, Acta Mater. **51**, 4761 (2003).

[21] M. Haataja and F. Léonard, Phys. Rev. B **69**, 081201 (2004).

[22] M. Haataja, J. Mahon, N. Provatas, and F. Léonard, Appl. Phys. Lett. **87**, 251901 (2005).

[23] S. Hu and L.-Q. Chen, Acta Mater. **52**, 3069 (2004).

[24] M. Tang, W. Carter, and Y.-M. Chiang, Annu. Rev. Mater. Res. **40**, 501 (2010).

[25] J. J. Hoyt and M. Haataja, Phys. Rev. B **83**, 174106 (2011).

[26] Y. Lu, C. Wang, Y. Gao, R. Shi, X. Liu, and Y. Wang, Phys. Rev. Lett. **109**, 086101 (2012).

[27] M. Tang and A. Karma, Phys. Rev. Lett. **108**, 265701 (2012).

[28] Y. Tao, C. Zheng, Z. Jing, D. Wei-Ping, and W. Lin, Chin. Phys. Lett. **29**, 078103 (2012).

[29] Z. Wang, J. Wang, S. Tang, Y. Guo, J. Li, Y. Zhou, and Z. Zhang, Philos. Mag. **93**, 2122 (2013).

[30] J. Cahn and J. Hilliard, J. Chem. Phys. **31**, 688 (1959).

[31] P.-A. Geslin, B. Appolaire, and A. Finel, Acta Mater. **71**, 80 (2014).

[32] P.-A. Geslin, Ph. D. thesis, Université Pierre et Marie Curie, 2013.

[33] N. Goldenfeld, B. P. Athreya, and J. A. Dantzig, Phys. Rev. E **72**, 020601 (2005).

[34] B. P. Athreya, N. Goldenfeld, and J. A. Dantzig, Phys. Rev. E **74**, 011601 (2006).

[35] R. Spatschek and A. Karma, Phys. Rev. B **81**, 214201 (2010).

[36] J. Berry, M. Grant, and K. R. Elder, Phys. Rev. E **73**, 031609 (2006).

[37] See Supplemental Material at http://link.aps.org/supplemental/10.1103/PhysRevLett.114.105501 for details of the simulations and of the linear stability analysis.

[38] M. Tang, J. Belak, and M. Dorr, J. Phys. Chem. C **115**, 4922 (2011).

[39] J. Cahn, Acta Metall. **5**, 169 (1957).

[40] S. Hu and L.-Q. Chen, Acta Mater. **49**, 463 (2001).

[41] F. Léonard and M. Haataja, Appl. Phys. Lett. **86**, 181909 (2005).

[42] J.-C. Zhao and M. Notis, Acta Mater. **46**, 4203 (1998).

[43] F. Bitter, Phys. Rev. **37**, 1527 (1931).

[44] P. Fratzl, O. Penrose, and J. Lebowitz, J. Stat. Phys. **95**, 1429 (1999).

[45] R. Asaro and W. Tiller, Metall. Trans. **3**, 1789 (1972).

[46] M. Grinfeld, Sov. Phys. Dokl. **31**, 831 (1986).

[47] Lambert W_L function is defined as the inverse function of x: $\rightarrow xe^x$, i.e., $W_L(xe^x) = x$.

[48] A. Koul and G. Gessinger, Acta Metall. **31**, 1061 (1983).

[49] R. Mitchell, H. Li, and Z. Huang, J. Mater. Process. Technol. **209**, 1011 (2009).

[50] M. Cottura, B. Appolaire, A. Finel, and Y. Le Bouar, Acta Mater. **72**, 200 (2014).